

Radio analysis of a system of radio galaxies (including a wide angle tail galaxy) in the Cosmos field at redshift $z=0.35$

Paula Vulić

Supervisor: prof. dr. sc. Vernesa Smolčić

Department of Physics, Faculty of Science, University of Zagreb, Bijenička 32, Zagreb

(Dated: January 22, 2022)

Abstract

Wide angle tail (WAT) radio galaxies are commonly located in galaxy clusters or groups. Their bent shapes indicate an interaction during a relative motion between their jets and the surrounding intracluster medium. Here, we perform a radio analysis of a system of two close radio galaxies in the COSMOS field: COSMOSVLA3 J100026.49+024229.7 (hereafter 44, according to the ID from the catalog at 3 GHz) and COSMOSVLA3 J100028.28+024103.3 (hereafter 10913), second of which is undoubtedly the WAT galaxy. Additionally, we analyze a third radio galaxy close-by, COSMOSVLA3 J095946.30+023602.1 (hereafter 187) potentially forming a bound system with the first two at a redshift of $z \approx 0.35$. The analysis is done using radio data at 4 different frequencies: 3 GHz, 1.4 GHz, 610 MHz, and 325 MHz. We overlay their radio contours with near-infrared (NIR) images of the sources' host galaxies. We investigate a spatial distribution of energy of emitting plasma in the sources by obtaining and analyzing 3 GHz - 1.4 GHz spectral index maps. Both, using their radio contours, and the spectral index maps we find that two of the sources, 44 and 187 are classified as FRI, whereas one of them, 10913 is an FR II type. We calculate the total radio luminosity for all three radio galaxies yielding $1.26 \times 10^{51} \text{ W Hz}^{-1}$, $1.15 \times 10^{50} \text{ W Hz}^{-1}$, and $3.43 \times 10^{50} \text{ W Hz}^{-1}$ for 10913, 44 and 187 respectively. Finally, the effect of relativistic beaming is examined in detail for radio galaxy 44. Assuming that this galaxy is the WAT, we limit the Doppler (de)boosting factor and estimate that in the case of maximal relativistic beaming, the total observed combined luminosity of jets is ≈ 6 times larger than the total intrinsic combined luminosity.

1. INTRODUCTION

1.1. Emission from radio sources

Active Galactic Nuclei (AGN) are highly luminous sources, detected over the whole electromagnetic spectrum whose emission is believed to be the result of accretion onto supermassive black holes (SMBH) of the corresponding galaxies¹². Radio galaxies, being the type of AGN with the strongest emission in radio wavelengths, are an important topic in astrophysics. Their radio luminosity is mostly due to the synchrotron radiation i.e. emission from relativistic electrons moving in a magnetic field²⁶ as illustrated in the top panel of Fig 1.

The synchrotron emission that we observe is a superposition of emission from single electrons²⁰. It's linearly polarised, and it has a continuum spectrum with the flux density (flux per unit frequency F_ν) value depending on a frequency (ν) according to²³:

$$F_\nu \propto \nu^{-\alpha} \quad (1)$$

In the expression above, α is defined as spectral index, and is a measure of the radio spectral energy distribution (SED) slope in the log-log plane²³:

$$\alpha = -\frac{\partial \log F_\nu}{\partial \log \nu} \quad (2)$$

which easily follows from the equation (1). The spectral index is often defined in the opposite sign convention. Since in the latter case, the typical spectral index values for radio galaxies are negative, here we prefer to use

the convention of equation (1). The spectral index is an important tool in the radio analysis of sources. It is commonly used to distinguish between different mechanisms of radio production in sources. A steep spectrum is due to the synchrotron emission of relativistic electrons, while a flat spectrum (small values of α) is a sign of a thermal bremsstrahlung emission from HII regions⁶, but is also typical for the synchrotron emission in a central AGN re-

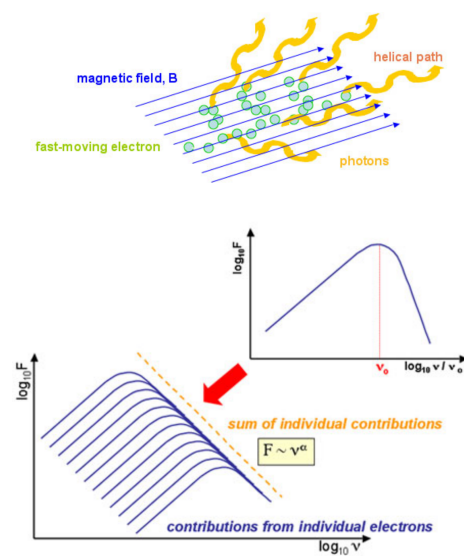


Figure 1: Electrons in plasma follow helical paths, emitting synchrotron radiation. Image credits: Swinburne University of Technology²⁰

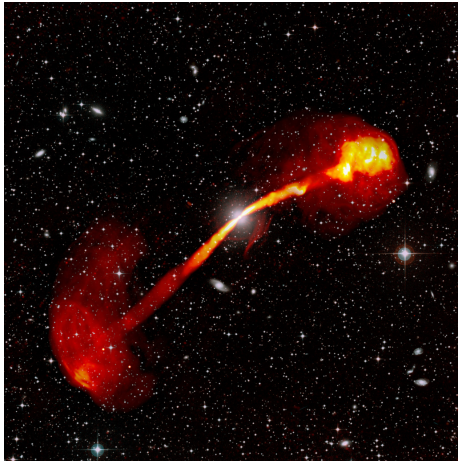


Figure 2: Radio galaxy hosted by bright and massive elliptical IC 4296 galaxy. Radio data (red) shown is from the South African Radio Astronomy Observatory's MeerKAT telescope, and is superimposed on the optical image (black-white scale). Adapted from: Condon et al.⁴

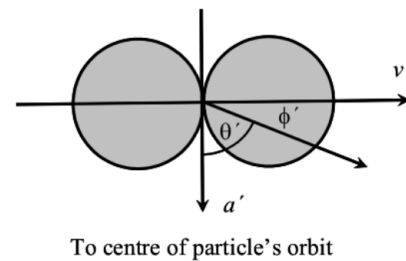
gion of radio galaxies. Along with the radio synchrotron radiation, the inverse-Compton process plays an important role in forming the total observed emission. This is a consequence of relativistic electrons interacting with photons, and causing them to Thompson-scatter to high energies²⁶ (visible in optical and/or X-ray).

1.2. Extended components and different radio morphologies

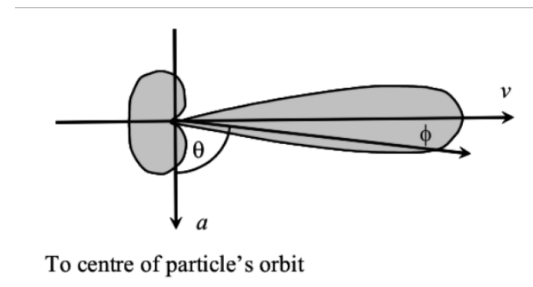
Radio sources can be classified as point sources or extended sources, depending on the extent of their radio emission. Furthermore, for extended radio morphologies the Fanaroff-Riley (FR) classification exists²⁴, dividing sources to edge-darkened (FR-I) or edge-brightened (FR-II). The extended components of radio galaxies are jets, hotspots, and lobes. Figure 1. displays the radio galaxy IC 4296, highlighting all of the mentioned radio features. Jets are narrow and long radio features originating from collimated flows of charged plasma flowing out from the central AGN. The radio jets are feeding lobes - clouds of diffuse radio emission, mostly coming in pairs and placed on either side of the active nucleus²⁶. The jets of very luminous sources often terminate in bright hotspots in the lobes. The appearance of the bright hotspots, which are usually seen in FR-II sources, is believed to be a manifestation of shocks, formed when the high-velocity jet (speeds higher than the speed of sound in plasma) abruptly terminates at the end of the source⁵. Sometimes, the whole structure, both radio jets, and lobes are referred to as simply jets.

1.3. Relativistic beaming effect

It may happen that that one jet of the extended radio source is visible and the other one is visible but much fainter or not detected at all. This is due to the relativistic beaming effect¹³. The electrons of plasma moving in the magnetic field are emitting synchrotron radiation perpendicular to their acceleration (Figure 3.) i.e. along the velocity direction since they are spiraling around the magnetic lines. The observed power of the radiation depends on the projection of the acceleration perpendicular to the line of sight i.e. depends on the observing angle with the respect to the electron acceleration direction. In the electron's rest frame the radiation is emitted symmetrically through two equal lobes, forward and back-going lobe spreading along or against the velocity direction (top of Fig 3.). If the electron is moving with a relativistic speed relative to the laboratory frame, the forward-going lobe is elongated along the direction of motion, while the back-going lobe is stretched (bottom of Fig 3.). Further-



To centre of particle's orbit



To centre of particle's orbit

Figure 3: Visualization of the relativistic beaming effect. The figure shows synchrotron emission from a particle in a circular motion. At the top, the particle is shown in its rest frame, and radiation is emitted through two equal lobes. Angles $\phi' = \pm\pi/4$ in the rest frame represent the angles at which the radiation intensity falls to half its maximum value. At the bottom, the emission is shown in the laboratory frame moving relativistically with the respect to the particle's frame. The forward-going lobe is elongated and carries most of the radiation energy. The back-going lobe is stretched and carries a neglectable amount of energy. The corresponding angles ϕ in the laboratory frame are $\sin\phi \approx \phi \approx 1/\gamma$, where $\gamma = 1/\sqrt{1-(v/c)^2}$ is the relativistic factor. Image credits: the Beckmann's lectures¹.

more, due to the Doppler shifting effect, the forward-going lobe carries most of the emitting power from the laboratory frame perspective. Once again, the observed

emission is a superposition of the emission from single electrons experiencing this effect. This is called the relativistic beaming effect (sometimes referred to as Doppler boosting) and causes modifications in the apparent luminosity of the emitting matter²⁵.

1.4. Cluster and group indicators

Radio galaxies are often located in galaxy groups or clusters and are therefore used as their indicators, especially at large redshifts where other methods fail in precision and sensitivity¹⁶. The optical galaxy hosting the radio source (the host galaxy) is usually a massive elliptical galaxy placed at the bottom of the gravitational potential well of a surrounding cluster and coinciding with the cluster's center of mass. However, the latter is not the case in dynamically young clusters i.e. clusters that experienced merging events in the recent past or are experiencing ongoing merger events¹⁶. The presence of an intracluster medium (ICM), filling the space between the galaxies, is another indicator for the existence of a cluster potential well. The environments of radio sources are usually analyzed using optical and X-ray data.

1.5. Wide angle tail galaxies

Radio galaxies span a wide range of shapes i.e. structures in the radio maps. One special type are the so-called wide-angle tail (WAT) radio galaxies. These are usually found in galaxy clusters, and their jets appear bent forming a C shape¹⁷. According to the results from the previous work the bending is usually due to the interaction with the ICM². Previous studies on WAT galaxies show that their host galaxy is usually the most luminous one in the cluster (Burns³), and is misplaced from its mass center (Sakelliou et al.¹⁴). Several WAT galaxies and their environments have been investigated in the COSMOS field (Smolčić et al.¹⁷, Oklopčić et al.¹¹). In these studies, environment analysis showed indications of group merger events i.e. signs of intensive dynamics.

Here, we present the radio analysis of a system of two close by radio galaxies from the COSMOS field: 44 and 10913. Both of these galaxies are located at a redshift of $z \approx 0.35$, and radio galaxy 10913 is undoubtedly the WAT. Additionally, we examine a third, radio galaxy 187

from the same field, located close to our two-galaxies system, and approximately at the same redshift. We show radio contours at different frequencies, and overlay them with the optical/NIR background in section 3.1. As a part of the radio analysis, we construct and analyze the spectral index maps for our sources in section 3.2. In section 3.3, the total 3 GHz radio luminosities are calculated from the flux density values. We estimate the relativistic beaming effect for radio galaxy 44 in section 3.4.

Radio sources analyzed here were chosen based on their mutual closeness and morphology (all sources are extended objects, and at least one is WAT galaxy). This suggests that galaxies may be hosted by mutually close galaxy groups, some of which could possibly be classified as dynamically young. The latter opens a question of groups dynamics as well as possible gravitational interaction between different groups, therefore encouraging further research. The process of identifying the galaxies of interest is described in detail in section 2.2.

2. DATA AND METHOD

The galaxies analysed here were chosen from the two square degree COSMOS field centered on right ascension $RA = 10^h 00^m 28.6^s$ and declination $DEC = +02^\circ 12' 21.0''$. The names, coordinates, redshifts and other properties of the galaxies are shown in the Table I.

Radio flux density maps are the main data source for the radio analysis, which here, for each of the sources, includes finding the radio contours, obtaining the spectral index maps, and calculating a total radio luminosity. For radio galaxy 44, analysis additionally includes the estimation of the relativistic beaming effect. We use flux densities from four radio continuum maps at different frequencies (3 GHz, 1.4 GHz, 600 MHz, 325 MHz). The 3 GHz (VLA-COSMOS 3 GHz continuum mosaic) and 1.4 GHz (VLA-COSMOS Deep 1.4 GHz mosaic) flux density data are taken from the VLA-COSMOS 3 GHz Large Project¹⁸ and VLA-COSMOS Deep Project respectively¹⁵. The former was constructed from 384 h of Very Large Array (VLA) observations of the COSMOS field and is characterized by 0.75'' resolution, and an average 2.3 $\mu\text{Jy}/\text{beam}$ rms noise. The latter was created from the VLA observations of 50'x 50' central region of the COSMOS field, reaching a resolution of 2.5'', and an average rms noise of $\approx 12 \mu\text{Jy}/\text{beam}$.

3 GHz ID	name	RA	DEC	zbest 3GHz	3 GHz multi	1.4 GHz multi	610 MHz multi	325 MHz multi
10913	COSMOSVLA3 J100028.28+024103.3	150.117854	2.684271	0.349	yes	yes	x	x
44	COSMOSVLA3 J100026.49+024229.7	150.110399	2.708261	0.344	no	yes	x	x
187	COSMOSVLA3 J095946.30+023602.1	149.942948	2.600608	0.351	no	yes	no	no

Table I: Sources and their properties from the 3 GHz, 1.4 GHz, 610 MHz, and 325 MHz catalog. The 10913 and the 44 are not detected in catalogs at MHz frequencies. Nevertheless, they are visible in the corresponding maps (Fig 8., 9., 10.)

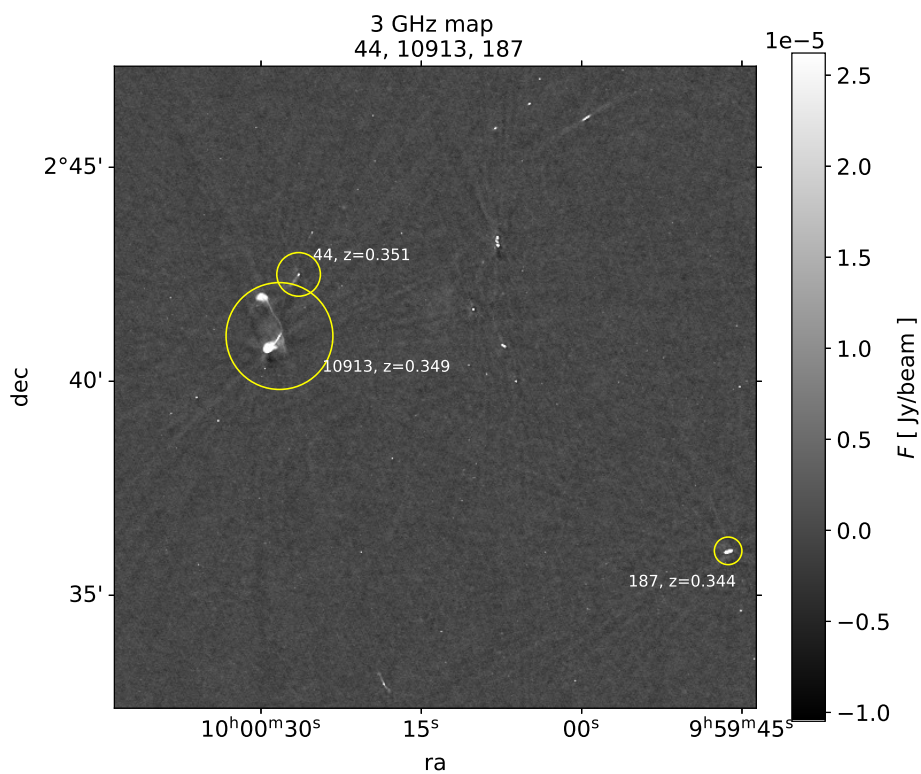


Figure 4: 3 GHz radio contours for sources of interest: 44, 10913, 187.

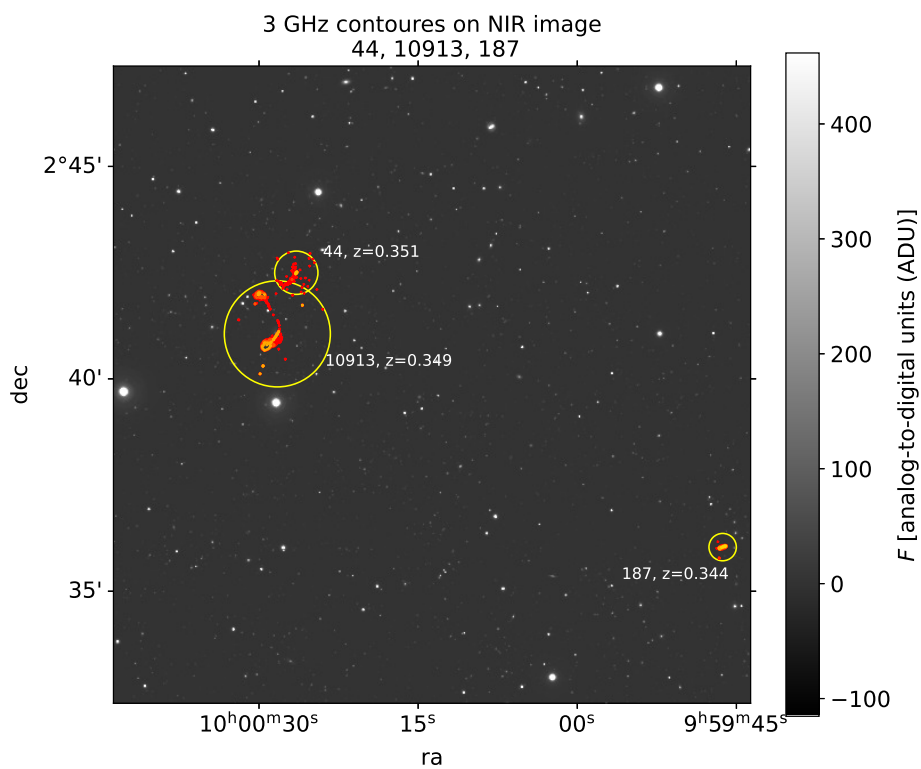


Figure 5: 3 GHz radio contours superimposed on the NIR image from the UltraVISTA for sources of interest: 44, 10913, 187.

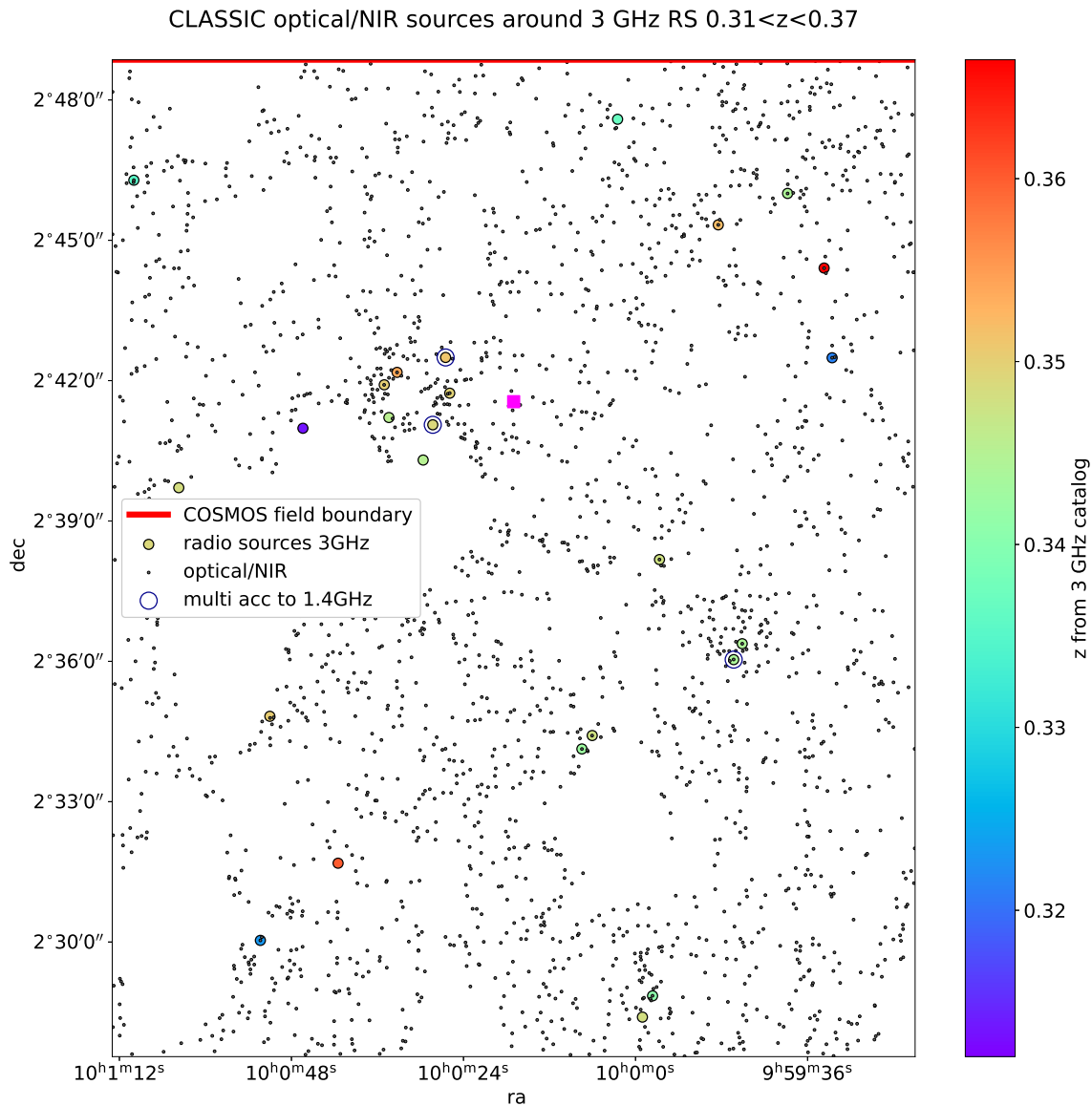


Figure 6: 3 GHz radio sources (colorful circles) plotted over the non-masked optical sources (gray points) from the COSMOS2020 CLASSIC photometric catalog with z in range 0.31 - 0.37. Holes in optical (i.e. missing) data are due to the presence of bright foreground stars. Magenta square marks the central coordinates of a $28' \times 28'$ optical box i.e. $27' \times 27'$ radio box. The red line marks the end of the COSMOS field i.e. the data boundary that happens to lay inside the optical i.e. the radio box of interest. Dark blue circles represent our sources. The overdensity of galaxies around the radio sources is evident.

The 325 MHz and 610 MHz radio continuum maps were obtained with the Giant Meter Radio Telescope (GMRT), and are described in Tisanic et al.²¹ The 325 MHz map was constructed from 45 hours of observations at a resolution of $10.8'' \times 9.5''$ and has a median rms noise of $97 \mu\text{Jy}/\text{beam}$, while the 610 MHz observations lasted for 86 hours and resulted in a resolution of $5.6'' \times 3.9''$,

and a median rms of $39 \mu\text{Jy}/\text{beam}$. Hereafter, the radio continuum mosaics will be referred to as the 3 GHz, 1.4 GHz, 610 GHz, and 325 GHz maps. Additionally, we use rms noise maps joined to the radio maps and obtained as a part of the related projects^{15,18,21}, as well as the corresponding radio source catalogs. Exceptionally, at 3 GHz we use the COSMOS VLA 3GHz Multiwavelength Coun-

terpart Catalog¹⁹ (3 GHz catalog hereafter). To identify radio sources of interest we work with both, data from radio and optical source catalogs. Optical data is taken from the recently published photometric catalogs²² COSMOS2020 CLASSIC and COSMOS2020 FARMER. Redshift values used here are photometric and are adopted from the 3 GHz catalog for the radio sources i.e. from the FARMER and CLASSIC for optical sources. Finally, to place the radio contours in the context of the optical/NIR background we overlay them over the source images cut from UltraVISTA maps obtained at NIR wavelengths¹⁰.

2.1. Identifying radio sources of interest and their optical counterparts

The system of two, close by radio galaxies with interesting morphologies (44 and 10913) was detected by looking into the 3 GHz map. The 3 GHz catalog recognizes these bright radio galaxies as one-component and multi-component sources respectively for the 44 and 10913 and places them at the approximately same redshift $z \approx 0.35$ (see Table I. for the exact values).

By cross-matching the 3 GHz catalog with the other three catalogs at lower frequencies, we find that our sources are also detected and both classified as multi-component at 1.4 GHz (see Table I.). We search the neighbourhood for additional radio galaxies by filtering for radio sources within $27' \times 27'$ box centered on $RA = 10^h 00^m 17^s$, $DEC = +02^\circ 41' 33.0''$, and with a redshift value between $0.31 < z < 0.37$, from the 3GHz catalog. Acceptable redshift range was calculated as $z_{mean} \pm \Delta z$ where z_{mean} is the mean redshift value for three sources, and Δz is determined according to:

$$\Delta z = 3 \sigma_{\delta z/(1+z)} \cdot (1 + z_{mean}) \quad (3)$$

with $\sigma_{\delta z/(1+z)} = 0.7\% = 0.007$ being the typical photometric redshift error for our sources. Except for the 44 and 10913, we found 24 sources matching the criteria, giving a total of 26 radio sources. Only one of them, COSMOSVLA3 J095946.30+023602.1 (hereafter 187, according to the 3 GHz catalog ID) is classified as the multicomponent source according to the 1.4 GHz catalog. Crossmatching shows that the radio galaxy 187 is detected at all 4 radio wavelengths. Fig 4. displays these three, multicomponent sources with their 3 GHz radio contours. The same contours are plotted over the NIR image from the UltraVISTA¹⁰ in Fig 5. Radio contours are examined in detail in section 3.1. Additionally, we search the sky area of interest at optical wavelengths. Optical sources were extracted from the COSMOS CLASSIC and COSMOS FARMER catalogs within a $28' \times 28'$ box centered on the same coordinates that were used in searching for radio sources. Again, optical data is filtered for the redshift value between $0.31 < z < 0.37$. The optical box size is $1'$ larger in both spatial directions to avoid boundary difficulties

when analyzing for the increase in the local galaxy density value. By looking at the filtered optical data from COSMOS CLASSIC superimposed on the previously extracted 26 radio sources (Fig 6.) we find the signs of possibly increased local galaxy density around the radio sources, including our radio galaxies (blue circles). This is expected for the reasons described in section 1.4. Using the FARMER data instead, we obtain the similar result. However, reporting the increase in galaxy density requires more detailed optical analysis, which is beyond the scope of this work. The signs of possible increase in galaxy density, mutual closeness, and the extended and interestingly shaped morphology make the 44, 10913, and 187 radio galaxies our sources of interest for the presented analysis.

To visualize and read the data from the radio maps Python Astropy and Matplotlib packages, as well as the SAO Image DS9 software, was used. With the help of Matplotlib, combined with the World Coordinate System (WCS) package, we produce the final graphs. Python Pandas package and TOPCAT software are employed for radio and optical catalog manipulations (filtering, cross-matching, and extracting specific catalog data).

2.2. Radio contours

To find the radio contours (and to perform the further radio analysis) we cut out images of our radio sources from the flux density maps at four different frequencies (3 GHz, 1.4 GHz, 610 MHz, 325 MHz). For each of the source images, we also cut out the noise image spanning the same area from the corresponding rms noise map. Calculating the median pixel value in the noise image, we find the median local rms noise value.

In the process of generating the contours (i.e. curves of constant flux density), we start by setting up contour models for each of the sources. This includes specifying the contour scale (logarithmic or linear), setting the lowest detectable flux density, and the number of contours. Iteratively, we converge at a model that gives the clearest results i.e. contours that are the easiest to distinguish from each other. Furthermore, for each of the sources, we plot 3 GHz contours over a NIR image (UltraVISTA data). Both, cutting from maps and radio contouring are performed using Python (Astropy, Pandas, and Matplotlib packages). Additionally, to produce the final images, the Python WCS package is used.

2.3. Spectral index maps

For each of the sources a spectral index map has been created by calculating a pixel by pixel spectral index value according to the formula that follows from equation (1):

$$\alpha_{\nu_1\nu_2} = -\frac{\log F_1 - \log F_2}{\log \nu_1 - \log \nu_2} \quad (4)$$

Here ν_1 and ν_2 are two different observing frequencies. F_1 and F_2 are corresponding flux density values from source maps. From these maps, we retained only those pixels that have values above three times the local rms noise in each map. All pixels below this threshold were masked. We followed this procedure for the 3 GHz - 1.4 GHz frequency combination.

Since different radio maps are characterized by different frequencies, and therefore different resolutions, we first had to smooth the 3 GHz source images to match the coarser 1.4 GHz resolution. This was done by convolving the 3 GHz images to a $2.5''$ circular beam. Furthermore, we regridded the 3 GHz source images to exactly match the 1.4 GHz maps. Both smoothing and regridding were done using the CASA astronomy software⁷ (imsmooth and imregrid functions). Additionally, in the final spectral index maps, we masked all pixels with negative values since they appeared next to the source boundary and were likely to be a result of boundary issues.

2.4. Total radio luminosity

In order to calculate total radio luminosity at 3 GHz we used the expression:

$$L_{3 \text{ GHz}} = \frac{F_{3 \text{ GHz}} 4\pi D_L^2}{(1+z)^{1-\alpha}} \quad (5)$$

Here, $F_{3 \text{ GHz}}$ is a total flux density calculated by summing up the values of pixels covering the extended radio source, and dividing by the beam size in pixels. Only pixels with the value $> 4\sigma$ were taken into account. We find the beam size in pixels by dividing the beam area by the area of one pixel ($0.2 \times 0.2 \text{ arcsec}^2$) in the 3 GHz map. The beam area (in arcsec) is calculated as: $2\pi\sigma^2$, where σ can be obtained from the full width half maximum (FWHM) of the circular beam ($0.75''$ for 3 GHz map) as: $\sigma = \text{FWHM}/(2\sqrt{2\ln 2})$. Furthermore, α is the median spectral index value (defined by equation (1), and calculated in section 3.2.), and z is the redshift (we use photometric redshift from the 3 GHz catalog). Finally, D_L is the average luminosity distance dependent on the value of z , H_0 Hubble constant, and cosmological parameters (Ω_M , Ω_λ). D_L was calculated with the help of the Ned Wright's cosmology calculator²⁷, assuming the Benchmark model of the universe ($H_0 = 69.6 \text{ km s}^{-1} \text{ Mpc}^{-1}$, $\Omega_M = 0.286$, $\Omega_\lambda = 0.714$).

2.5. Relativistic beaming estimation

Jets of radio galaxies are intrinsically symmetric and relativistic radio features, and any exceptions from this are rare and easily recognizable, according to the previous work (Laing et al.⁹). Therefore, any apparent differences between the jet's luminosities can be assigned to relativistic effects i.e. to the relativistic beaming (otherwise called Doppler boosting, described in section 1.3.).

Here, we use both, the symmetry and relativistic nature as the main assumptions in estimating the Doppler boosting for radio galaxy 44. The symmetry allows us to describe the jet speeds associated with the beaming effect by a single jet speed for a given source. This relativistic velocity in WAT galaxies can range between $0.3c - 0.7c$, according to the statistical study of a sample of 30 WAT galaxies (Jetha et al.⁸). Moreover, using the same symmetry, we can assume that both jets cover the same area, and their intrinsic luminosities L_0 are the same. However, due to the Doppler boosting effect, there is an increase in the observed luminosity of the approaching jet L_ν^{app} , given by:

$$L_\nu^{app}/L_0 = \delta^{2+\alpha} = [\gamma(1 - \beta\cos\theta)]^{-(2+\alpha)} \quad (6)$$

whereas the receding jet has its flux suppressed i.e. its luminosity L_ν^{rec} is given by:

$$L_\nu^{rec}/L_0 = \delta^{2+\alpha} = [\gamma(1 + \beta\cos\theta)]^{-(2+\alpha)} \quad (7)$$

Here, $\beta = v/c$ with v expressed in the units of the speed of light c , $\gamma = 1/\sqrt{1 - \beta^2}$ is the relativistic factor, α is the spectral index (consistent with the sign convention of equation (1)), θ is the jet orientation angle with respect to the line of sight, and δ is the Doppler factor.

Assuming the intrinsic luminosities of the approaching and receding jets are the same, we obtain a ratio of their observed luminosities (flux densities) R by dividing the equation (6) by equation (7):

$$R = L_\nu^{app}/L_\nu^{rec} = F_\nu^{app}/F_\nu^{rec} = \left(\frac{1 + \beta\cos\theta}{1 - \beta\cos\theta}\right)^{2+\alpha} \quad (8)$$

Using the observed total flux densities of the jets i.e. the ratio R , and knowing the spectral index value of the jets, it is possible to calculate $\beta\cos\theta$. Placing the limits on (or estimating) the jet's velocity then gives us the information on the orientation angle θ , and vice versa.

3. RESULTS

3.1. Radio contours

Radio contours overlaid onto radio maps at different frequencies (3 GHz, 1.4 GHz, 610 MHz, 325 MHz) for radio galaxies 44, 10913, and 187 are shown in Fig 7., Fig 8. and Fig 9. respectively. Contour model details are indicated in each plot.

Radio galaxy 44 Radio galaxy 44 has only one jet visible, extending towards the south-east. This is likely due to the relativistic beaming (see sections 1.3 and 2.5.). The jet is slightly bent towards the north (best visible at 1.4 GHz, upper right panel in Fig 7.). Taking the jets' symmetry (previously discussed in 2.5.) into account, this galaxy may be the WAT galaxy. Contours show that the

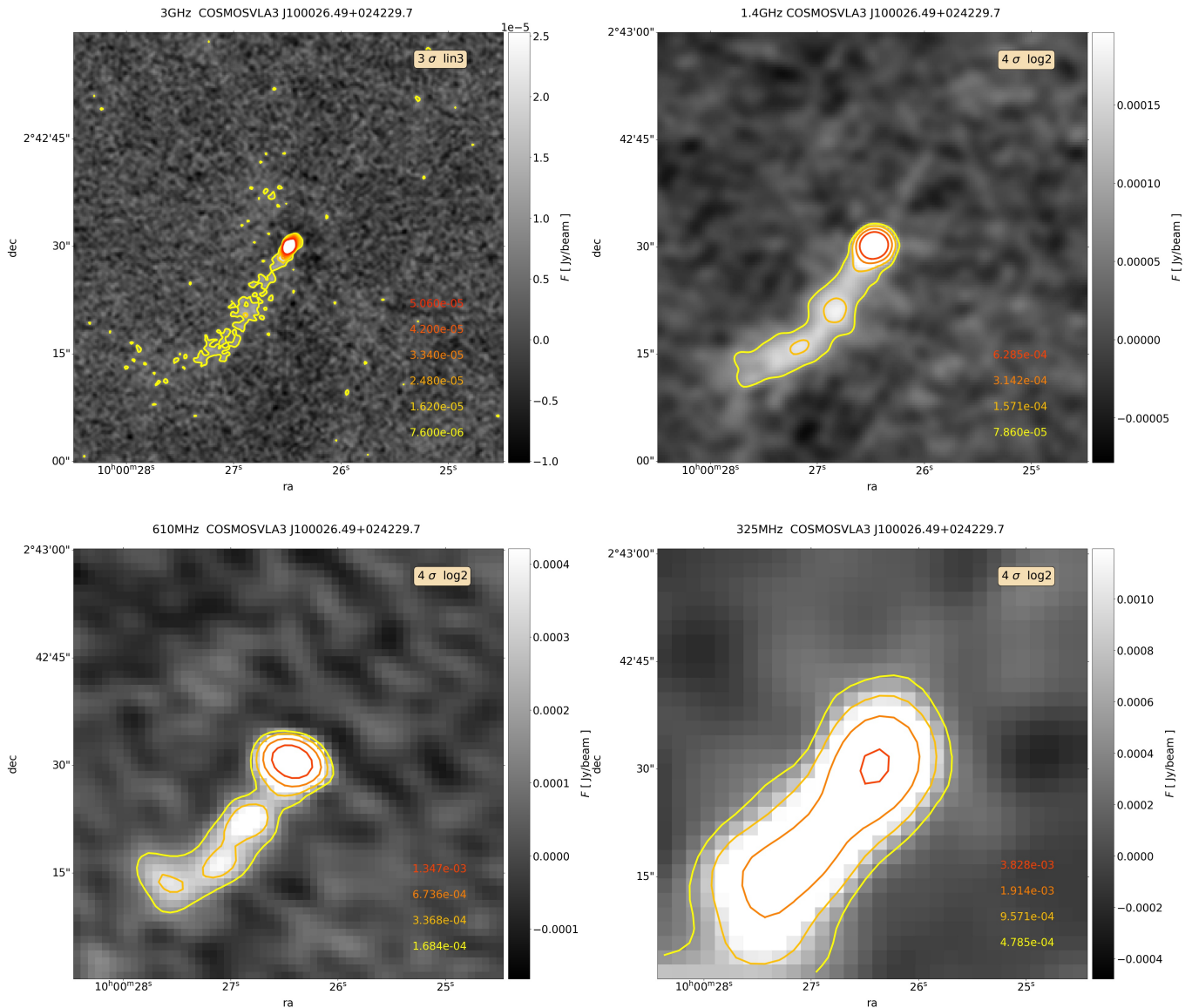


Figure 7: Radio contours for source 44 at four different frequencies. Label in the upper right corner of each image shows details of the radio contour model. It indicates the flux density value at which contours start and scale: logarithmic scale with base 2 (\log_2), or linear (lin N) scale where N is linear step value. At 3 GHz contour level values follow linear scale with linear step 8 (upper left panel), while at the remaining three frequencies logarithmic scale with base 2 gives much clearer results. Image scale is from -4σ - 10σ . Different contours are plotted in different colors, and corresponding level values are given, in the same colors in the corner of each image.

flux density significantly decreases from the central AGN towards the end of the jet. This implies we are dealing with the source of type FRI. The resolution is better at higher frequencies, enabling more detailed insight into radio features forming this extended source. At 1.4 GHz, 610 MHz, and 325 MHz we used 4σ as a contour starting point, where σ is the local rms noise (see section 2.2). Using this as a starting point at 3 GHz would leave us with a fewer lines contouring the jet. Therefore we set 3σ as a lower boundary and used a linear scale with step 8. At other frequencies (and at all frequencies for other

sources) we preferred to use logarithmic scale with base 2 (levels being 2^n with $n=2,3,4,\dots$)

Radio galaxy 10913 Central AGN together with two jets and lobes of the 10913 radio galaxy extends over $\approx 2.5''$ along the east-west direction, and over $\approx 90''$ along the north-south direction, spanning a much larger area on the sky plane than radio galaxy 44 (for visual comparison see Fig 4. and Fig 5.) Two jets originating from the central AGN are pointing north i.e. south. Both jets are bent toward the east. The latter may be

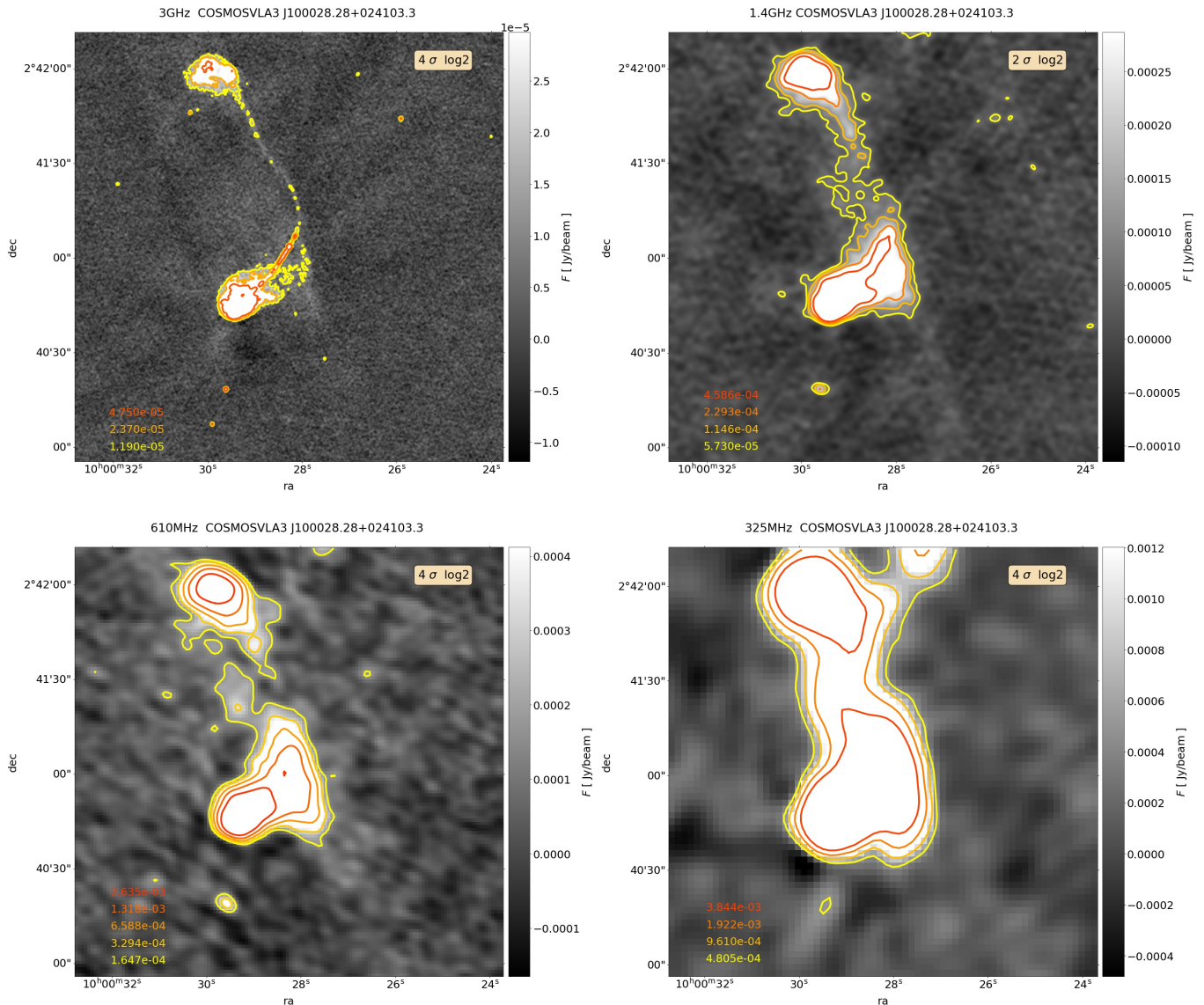


Figure 8: Contours for radio galaxy 10913 at 4 different frequencies. The labels in the upper right corners show the radio contour model details. At all frequencies, the logarithmic scale with base 2 gives the clearest results. Image scale is from -4σ - 10σ .

a consequence of a relative motion between the radio galaxy and the ICM of a possibly existing corresponding galaxy group (see section 1.4.). However, this requires further analysis in optical and X-ray. This galaxy is a very good example of a WAT. There is a noticeable asymmetry of the jets' luminosities that is likely due to the relativistic beaming effect (sections 1.3. and 2.5.). The central AGN is placed at RA $\approx 10^h 00^m 28.5^s$, DEC $\approx +02^\circ 41' 03''$. Contours show that the flux density is high (for example see the light orange line in the upper left panel of Fig 8.) in both, the central AGN region and in the lobes. Bright edges of the 10913 indicate this is the FR II type galaxy. Here, we produced all images using the \log_2 contour model with 4σ as the starting point except for the 1.4 GHz contours, where we used 2σ .

Radio galaxy 187 Different components of the 187 radio galaxy are best distinguishable at 3 GHz (upper left panel in Fig 9.) The existence of two different features originating from the central point (AGN) becomes evident by examining the contours obtained from this high-resolution image. Flux density values decrease as we move towards the edges, indicating this is the FR I type galaxy. All images in Fig 9. were created with contours starting from 4σ , and level values following a logarithmic scale with base 2.

We superimposed the 3 GHz radio contours on the NIR images from the UltraVISTA. This is shown in Fig 10., 11., and 12. for radio galaxies 44, 10913, and 187 respectively. One can infer that contours with the highest flux density value, that correspond to the central AGN, are

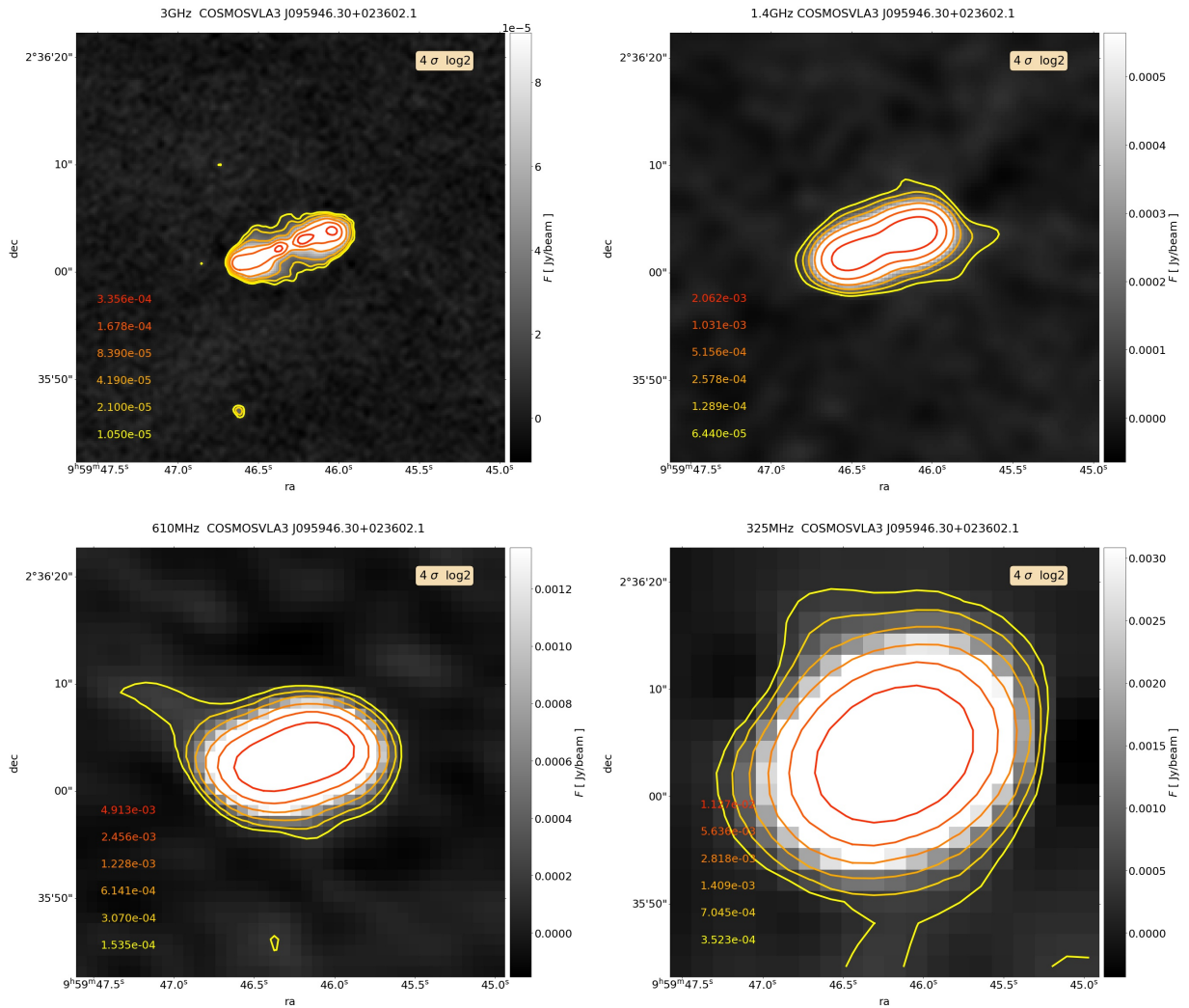


Figure 9: Contours for radio galaxy 187 at 4 frequencies. The label in the upper right corner of each image shows details of the radio contour model. At all frequencies, contour levels are best visible in log scale with base 2. Image scale is from -4σ - 35σ .

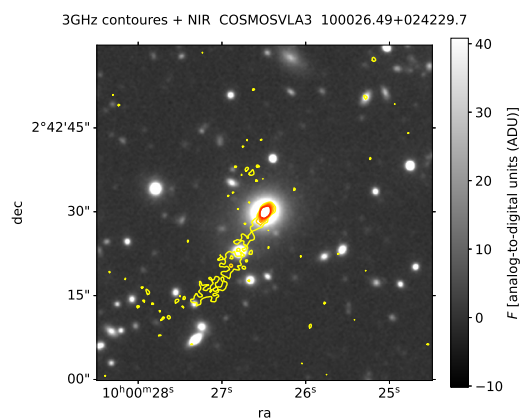


Figure 10: Radio contours overlaid on a NIR image for source 44. AGN is coinciding with the brightest galaxy in NIR - its host galaxy.

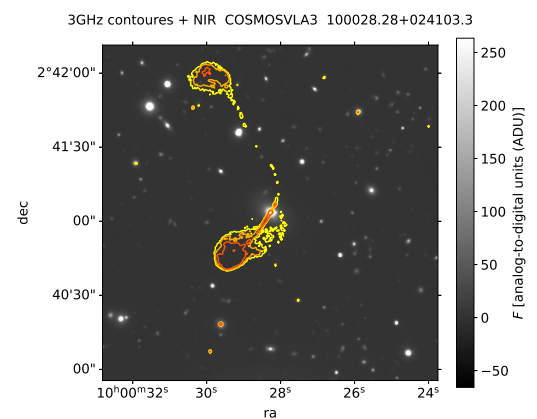


Figure 11: Radio contours overlaid on a NIR image for radio galaxy 10913. Central AGN is coinciding with the brightest NIR galaxy - its host galaxy.

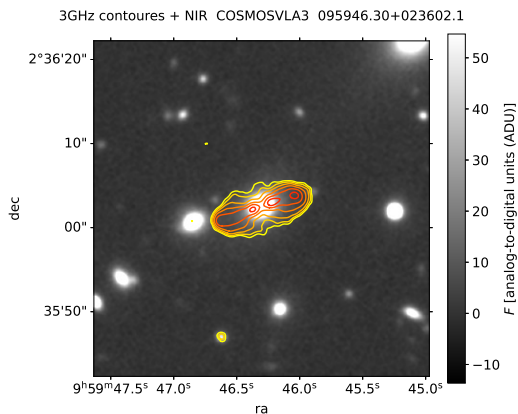


Figure 12: Radio contours overlaid on a NIR image for radio galaxy 187.

also coinciding with the peak in brightness i.e. with the center of the brightest source in NIR. This is in agreement with AGNs being located in the centers of optical/NIR galaxies, which are often the most luminous ones in the cluster or group.

3.2. Spectral index maps

As described in 2.3. section, we generated spectral index maps for our three sources. These were created using the 3 GHz and 1.4 GHz maps. Final index maps are shown in Fig 13., and are missing some parts (components) of the sources originally displayed in the previous figures. The reason is that all pixels below 3σ have been masked (section 2.3.). This was done to avoid problems i.e. peculiarities when calculating the spectral index, which can arise from including the pixels that are not covering the radio source but the surrounding noise or boundary area.

Radio galaxy 44 For radio galaxy 44 (mid-panel in Fig 13.) the radio spectrum of the AGN core is flat ($\alpha < 0.5$), and the spectral index value increases in the south-eastern jet (cloud). The flat spectrum of AGN cores is thought to be the result of self-absorption rather than a flat electron energy distribution⁶. On the jet's edges, the value reaches its maximum of ≈ 1.6 . The index value is generally lower not just around the AGN, but also in the central part of the south-eastern feature. Towards the edges, the spectrum becomes steeper which is a consequence of synchrotron and inverse Compton radiation losses (aging). This spatial distribution of index values again points towards an FRI classification. The median spectral index value is $\alpha_{med} = 1.196$.

Radio galaxy 10913 The radio galaxy 10913 (top panel in Fig 13.) has again the minimal spectral index value in the central AGN region. The values increase in

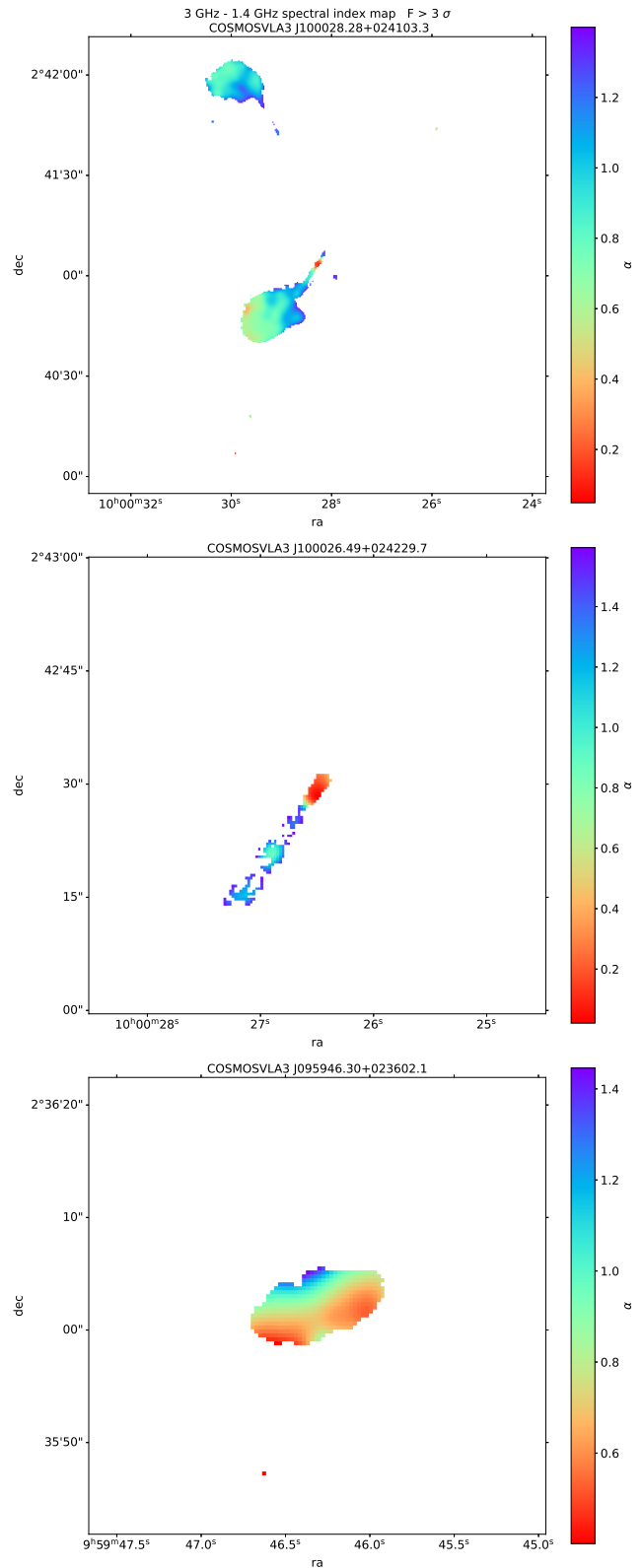


Figure 13: Spectral index maps for radio galaxies 44, 10913, and 187 created using 3 GHz and 1.4 GHz data(see section 2.3. for details)

the southern and northern lobes. Nevertheless, a low index values ($\alpha < 0.4$) can also be found in the eastern edge area of the southern lobe. The rest of this lobe is characterized by somewhat higher values but still mostly the flat spectrum ($\lesssim 0.65$). Moving inwards, from the southern lobe to the jet, and AGN (especially in the western part of the lobe) the values stepen progressively ($0.8 < \alpha < 1.3$) with the spectral index reaching ≈ 1.3 at its western edge. In the northern lobe, the spectrum is generally stepper in comparison to the southern one. Spectral index values are here ranging between 0.5 around the north-eastern edge of the lobe, and ≈ 1.4 at its southern edge. This increasing spectral index trend from the outer edges of the lobe to its inner parts, jets and the central core corresponds to the FRII classification. This agrees with the previous classification based on radio contours (section 3.1.). The median spectral index value is $\alpha_{med} = 0.910$.

Radio galaxy 187 From a spectral index map of radio galaxy 187 (bottom panel in Fig 13.) one can infer that the large central part of both, eastern and western radio clouds is characterized by a flat spectrum ($\alpha \lesssim 0.65$). Closer to the outer edge of the source the plasma energy decreases, and the spectral index value increases. This increase is evident in the northern part of the source, where the index value reaches its maximum of ≈ 1.4 on the northern galaxy edge. On the contrary, the index value reaches its minimum on the southern galaxy edge, whereas the higher index values in the southern part of the galaxy are only visible in the edgy region between the eastern and western cloud. The latter might be a consequence of masking the pixels below 3σ . However, choosing 2σ as a lower flux density limit would leave us with a significant amount of noise in the map. Also, the trend of spectral index value increasing with the distance from the center is noticeable on the eastern and western edges of the source. This trend agrees with the FRI classification, which also arises from the analysis of radio contours (section 3.1.). The median spectral index value is $\alpha_{med} = 0.719$.

3.3. Total radio luminosity

Total radio flux densities and corresponding luminosities of the radio galaxies 44, 10913, and 187 have been calculated as described in section 2.4. and are listed in

3 GHz ID	$F_{3\text{ GHz}}^{>4\sigma}$ [μJy]	$F_{3\text{ GHz}}^{\text{catalog}}$ [μJy]	R	$L_{3\text{ GHz}}^{>4\sigma}$ [10^{50}W Hz^{-1}]
10913	29933	32090	6%	12.16
44	2489	2250	10%	1.15
187	9238	9294	0.6%	3.43

Table II: Total flux density and luminosity values for radio galaxies: 44, 10913 and 187.

Table II. Comparing the total radio flux densities to that from the 3 GHz catalog, one can infer that the values agree within 10% or less (exact deviation from the catalog values $R = |F_{3\text{ GHz}}^{>3\sigma} - F_{3\text{ GHz}}^{\text{catalog}}|/F_{3\text{ GHz}}^{\text{catalog}}$, is given in the Table II. for each of the galaxies). Deviations from the 3 GHz catalog total flux values are likely due to differences between our method used to determine pixels that contribute to the sum and the method used in the catalog construction¹⁹. Here obtained, total flux density value of radio galaxy 44 is used when estimating the relativistic beaming effect on its jets (see section 3.4.).

3.4. Estimation of relativistic beaming for radio galaxy 44

Radio galaxy 44 has only one, south-eastern jet visible. This is likely due to the Doppler de(boosting) that affects its jets (see sections 1.3. and 2.5.).

To estimate this effect, we first calculate the flux of the approaching jet $F_{3\text{ GHz}}^{\text{app}} \approx 320 \mu\text{Jy}$ by subtracting the total flux density of the AGN core from the total galaxy flux density (section 3.3.). Only pixels above 8σ from the 3 GHz map were taken into account when summing for the AGN flux. Since the counter-jet is not visible, we can only calculate an upper limit on its flux by multiplying a 4σ value by the estimate of the area that the jet covers. This area is assumed to be the same for both, the approaching and receding jet, based on the symmetry previously discussed in section 2.5. The calculation results in the total counter-jet flux density $F_{3\text{ GHz}}^{\text{rec}} \lesssim 262 \mu\text{Jy}$. From this flux values, we estimate the lower limit on the flux ratio $R = F_{3\text{ GHz}}^{\text{app}}/F_{3\text{ GHz}}^{\text{rec}} \gtrsim 1.2$. Using equation (8), with α being the median jet spectral index value (≈ 1.3 , obtained using the map data for the visible jet of radio galaxy 44), this yields $\beta \cos\theta \gtrsim 0.03$. Different combinations of the jet velocity β , and the orientation angle θ satisfy this relation. However, it is possible to place the limits on the jet velocity if we assume that the radio galaxy 44 is a WAT galaxy i.e. that the receding and approaching jets are forming a C shape. This is a reasonable assumption with regard to the jets' symmetry. As discussed in section 2.5., based on the research conducted on 30 WAT galaxies⁸ their bulk jet velocity is in range $0.3\text{ c} - 0.7\text{ c}$.

Using this, we find that the Doppler boosting factor $\delta^{2+\alpha}$ for the approaching jet can range from ≈ 1.7 (for $\theta = 50^\circ$) to ≈ 11 (for $\theta = 20^\circ$), whereas deboosting factor $1/\delta^{2+\alpha}$ of the receding jet ranges from ≈ 2 (for $\theta = 50^\circ$) to ≈ 16 (for $\theta = 20^\circ$). It is possible to see this in Fig 14. (top panel), where we plot Doppler boosting (solid lines) and deboosting (dashed lines) factor for different velocities and orientation angles. The gray dot-dashed lines in Fig 14. mark the boundaries of the range of the most likely velocities ($0.3 c - 0.7 c$). In the bottom panel of Fig 14. we enlarge the low-velocity part of the upper image to highlight that the plots obey the $\beta \cos\theta \gtrsim 0.03$ rule. For each plot, given the value of the orientation angle, velocity at the left end of the line corresponds to the extreme case of this relation. According to the here-set estimation of the de(boosting) factor, in the case of the maximal Doppler boosting ($\beta = 0.7$ and $\theta = 20^\circ$), the observed total combined luminosity of the jets is ≈ 6 times larger than their intrinsic combined luminosity ($2L_0$). However, we can retain the total luminosity values calculated in section 3.3., since the jet flux only makes $\approx 13\%$ of the total galaxy luminosity.

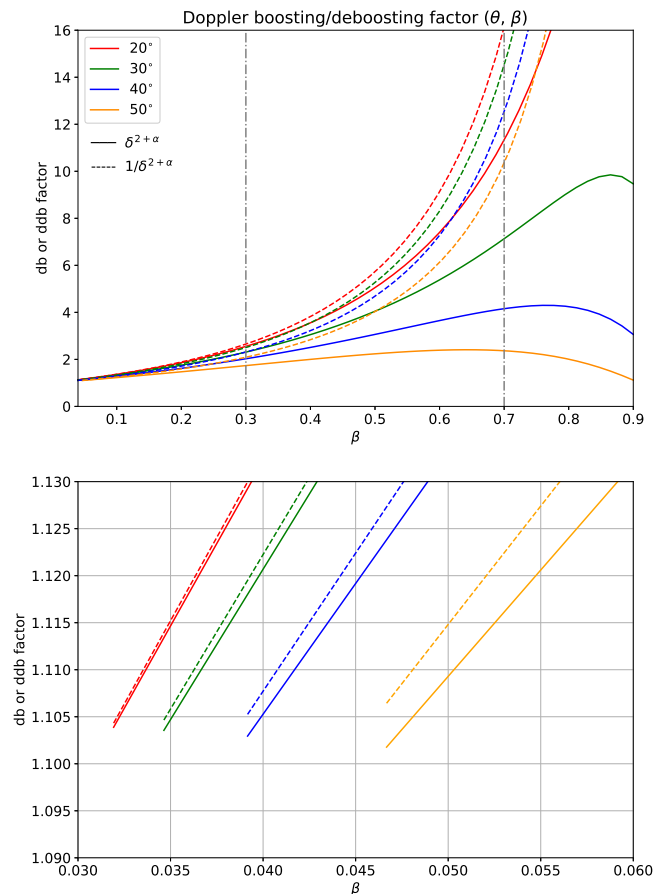


Figure 14: Doppler boosting (solid lines) and deboosting (dashed lines) factor at different velocities and orientation angles for the jets of radio galaxy 44. Gray dot-dashed lines bound the interval of the most likely jet velocities according to the Jetha et al.⁸

4. SUMMARY AND CONCLUSIONS

We performed the radio analysis of three multicomponent radio galaxies 44, 10913, and 187 from the Cosmos field using the radio data at 3 GHz, 1.4 GHz, 610 MHz, and 325 MHz. We show their radio contours at different frequencies, and overlay them with NIR images from the UltraVISTA. We create the 3 GHz - 1.4 GHz spectral index maps to study the spatial distribution of plasma energy in the galaxies. Using radio data at 3 GHz, we calculate their total monochromatic luminosities $L_{3 \text{ GHz}}$, and compare them to the values from the 3 GHz catalog. Finally, we estimate the relativistic beaming (Doppler boosting) effect on radio galaxy 44. The results of the here-presented analysis can be summarized as follows:

- Radio galaxies 44 and 187 are classified as FRI and galaxy 10913 is an FR II galaxy type, according to both, their radio contours and spectral index maps.
- Shape of the radio emission of galaxies 10913 and 44 suggest the former is, whereas the latter may be the WAT galaxy. The asymmetry of their jets' luminosities suggests that both galaxies are subjected to the relativistic beaming effect. Consequences of this are stronger in the case of radio galaxy 44. The emission of radio galaxy 187 is symmetric.
- The median spectral index values calculated from the corresponding 3 GHz - 1.4 GHz spectral index maps are 1.196, 0.910, and 0.719 for radio galaxies 44, 10913, and 187 respectively.
- Total 3 GHz luminosities are $1.26 \times 10^{51} \text{ W Hz}^{-1}$, $1.15 \times 10^{50} \text{ W Hz}^{-1}$, and $3.43 \times 10^{50} \text{ W Hz}^{-1}$ for radio galaxies 10913, 44 and 187 respectively. The values agree within 10% with the luminosities from the 3 GHz catalog.
- For the radio galaxy 44, the ratio of the jets' fluxes yields $\beta \cos\theta \gtrsim 0.03$. Assuming this is the WAT galaxy, the Doppler boosting factor for the approaching jet can range from ≈ 1.75 (for $\theta = 50^\circ$) to ≈ 11 (for $\theta = 20^\circ$), and deboosting factor for the receding jet from ≈ 2 to ≈ 16 for the same values of the orientation angle θ . The maximal estimated boosting results in the total observed combined jet luminosity being ≈ 6 times higher than the intrinsic one.

- ¹ V. Beckman. URL https://asd.gsfc.nasa.gov/Volker.Beckmann/school/download/Longair_Radiation2.pdf.
- ² M. C. Begelman, M. J. Rees, and R. D. Blandford. A twin-jet model for radio trails. *Nature (London)*, 279:770–773, June 1979. doi: 10.1038/279770a0.
- ³ J. O. Burns. The structure and environment of the wide-angle tailed radio galaxy 1919+479. *mnras*, 195:523–533, May 1981. doi: 10.1093/mnras/195.3.523.
- ⁴ J. J. Condon et al. Threads, Ribbons, and Rings in the Radio Galaxy IC 4296. *Astrophys. J.*, 917(1):18, August 2021. doi: 10.3847/1538-4357/ac0880.
- ⁵ James J. Condon and Scott M. Ransom. *Essential Radio Astronomy*. Princeton University Press, 2016. ISBN 9781400881161. doi: doi:10.1515/9781400881161. URL <https://doi.org/10.1515/9781400881161>.
- ⁶ F. de Gasperin et al. A radio spectral index map and catalogue at 147–1400 MHz covering 80 per cent of the sky. *mnras*, 474(4):5008–5022, March 2018. doi: 10.1093/mnras/stx3125.
- ⁷ International Consortium Of Scientists. CASA: Common Astronomy Software Applications, July 2011.
- ⁸ Nazirah N. Jetha et al. Jet speeds in wide-angle tailed radio galaxies. *mnras*, 368(2):609–618, May 2006. doi: 10.1111/j.1365-2966.2006.10155.x.
- ⁹ R. A. Laing et al. Asymmetries in the jets of weak radio galaxies. *mnras*, 306(3):513–530, July 1999. doi: 10.1046/j.1365-8711.1999.02548.x.
- ¹⁰ H. J. McCracken et al. VizieR Online Data Catalog: UltraVISTA Catalogue Release DR1 (McCracken+, 2012). *VizieR Online Data Catalog*, art. J/A+A/544/A156, August 2012.
- ¹¹ A. Oklopčić et al. A wide-angle tail galaxy at $z = 0.53$ in the COSMOS field. *memsai*, 82:161, January 2011.
- ¹² P. Padovani et al. Active galactic nuclei: what’s in a name? *aapr*, 25(1):2, August 2017. doi: 10.1007/s00159-017-0102-9.
- ¹³ A. Parsons. The basics of synchrotron emission, 2016. URL <https://youtu.be/FnYNjKbmxU>.
- ¹⁴ Irini Sakelliou and Michael R. Merrifield. The origin of wide-angle tailed radio galaxies. *mnras*, 311(3):649–656, January 2000. doi: 10.1046/j.1365-8711.2000.03079.x.
- ¹⁵ E. Schinnerer et al. The VLA-COSMOS Survey. IV. Deep Data and Joint Catalog. *apjs*, 188(2):384–404, June 2010. doi: 10.1088/0067-0049/188/2/384.
- ¹⁶ Peter Schneider. *Extragalactic Astronomy and Cosmology*. 2006.
- ¹⁷ V. Smolčić et al. A Wide-Angle Tail Radio Galaxy in the COSMOS Field: Evidence for Cluster Formation. *apjs*, 172(1):295–313, September 2007. doi: 10.1086/516583.
- ¹⁸ V. Smolčić et al. The VLA-COSMOS 3 GHz Large Project: Continuum data and source catalog release. *aap*, 602:A1, June 2017. doi: 10.1051/0004-6361/201628704.
- ¹⁹ V. Smolčić et al. The VLA-COSMOS 3 GHz Large Project: Multiwavelength counterparts and the composition of the faint radio population. *aap*, 602:A2, June 2017. doi: 10.1051/0004-6361/201630223.
- ²⁰ Swinburne University of Technology. URL <https://astronomy.swin.edu.au/cosmos/S/Synchrotron+Emission>.
- ²¹ K. Tisanić et al. The VLA-COSMOS 3 GHz Large Project: Average radio spectral energy distribution of highly star-forming galaxies. *aap*, 621:A139, January 2019. doi: 10.1051/0004-6361/201834002.
- ²² J. R. Weaver et al. COSMOS2020: A panchromatic view of the Universe to $z \sim 10$ from two complementary catalogs. *arXiv e-prints*, art. arXiv:2110.13923, October 2021.
- ²³ Wikipedia contributors. Spectral index — Wikipedia, the free encyclopedia, 2019. URL https://en.wikipedia.org/w/index.php?title=Spectral_index&oldid=913420392. [Online; accessed 28-December-2021].
- ²⁴ Wikipedia contributors. Fanaroff–riley classification — Wikipedia, the free encyclopedia, 2021. URL https://en.wikipedia.org/w/index.php?title=Fanaroff%E2%80%93Riley_classification&oldid=1036783010. [Online; accessed 26-December-2021].
- ²⁵ Wikipedia contributors. Relativistic beaming — Wikipedia, the free encyclopedia, 2021. URL https://en.wikipedia.org/w/index.php?title=Relativistic_beaming&oldid=1044617833. [Online; accessed 26-December-2021].
- ²⁶ Wikipedia contributors. Radio galaxy — Wikipedia, the free encyclopedia, 2021. URL https://en.wikipedia.org/w/index.php?title=Radio_galaxy&oldid=1047210526. [Online; accessed 26-December-2021].
- ²⁷ Wright E. L. A Cosmology Calculator for the World Wide Web, 2006. URL <http://www.astro.ucla.edu/wright/CosmoCalc.html>.